Estimating the effective Reynolds number in implicit large-eddy simulation

Ye Zhou
Lawrence Livermore National Laboratory, Livermore, California 94550, USA

Fernando F. Grinstein, Adam J. Wachtor, and Brian M. Haines
MS F644, Los Alamos National Laboratory, Los Alamos, New Mexico 87545, USA

(Received 10 July 2013; revised manuscript received 22 August 2013; published 13 January 2014)

In implicit large-eddy simulation (ILES), energy-containing large scales are resolved, and *physics capturing* numerics are used to spatially filter out unresolved scales and to implicitly model subgrid scale effects. From an applied perspective, it is highly desirable to estimate a characteristic Reynolds number (Re)—and therefore a relevant effective viscosity—so that the impact of resolution on predicted flow quantities and their macroscopic convergence can usefully be characterized. We argue in favor of obtaining robust Re estimates away from the smallest scales of the simulated flow—where numerically controlled dissipation takes place and propose a theoretical basis and framework to determine such measures. ILES examples include forced turbulence as a steady flow case, the Taylor-Green vortex to address transition and decaying turbulence, and simulations of a laser-driven reshock experiment illustrating a fairly complex turbulence problem of current practical interest.

DOI: 10.1103/PhysRevE.89.013303 PACS number(s): 47.11.−j, 47.27.Jv, 46.15.−x

I. INTRODUCTION

High Reynolds number (Re) turbulent flow complexity typically involved requires achieving accurate and dependable large-scale predictions of highly nonlinear processes with under-resolved computer simulation models. In large-eddy simulation (LES) [1], the large energy-containing structures are resolved, smaller structures are spatially filtered out, and unresolved subgrid scale (SGS) effects are modeled. A crucial practical LES computational aspect is the need to distinctly separate the effects of spatial filtering and SGS reconstruction models from their unavoidable implicit counterparts due to discretization. Indeed, it has been noted [2,3] that, in typical LES strategies, truncation terms due to discretization and filtering [4,5] have contributions directly comparable with those of the explicit models. Seeking to address the seemingly insurmountable issues posed to LES by under-resolution, the possibility of using the SGS modeling and filtering provided implicitly by the numerics has been considered as an option generally denoted as *numerical LES* (e.g., Pope [6]). Arbitrary numerics will not work for LES: *Good or bad* SGS physics can be built into the simulation model depending on the *choice of numerics and its particular implementation*.

The monotone integrated LES approach—first proposed by Boris [7] and Boris *et al*. [8], incorporates the effects of the SGS physics on the resolved scales through functional reconstruction of the convective fluxes using locally monotonic finite volume (FV) schemes. The more broadly defined implicit LES (ILES) [9] generally uses high-resolution nonoscillatory FV (NFV) algorithms to solve the unfiltered Euler or Navier-Stokes (NS) equations; popular physics capturing methods have been used in ILES, such as flux-corrected transport (FCT), the piecewise parabolic method, Godunov, hybrid, and total variation diminishing algorithms. By focusing on inertially dominated flow dynamics and regularization of under-resolved flow, ILES follows on the precedent of using NFV methods for shock capturing—requiring weak solutions and satisfaction of an entropy condition.

The utility of ILES for practical scientific and engineering simulations is clear. Indeed, even with today's powerful supercomputers, direct numerical simulation (DNS), where the physical kinematic viscosity ν is utilized and all the scales are resolved, are usually limited on how high a Re can be achieved. Here,

$$\mathrm{Re} = UL/\nu \tag{1}$$

is a basic parameter that describes the degree of nonlinearity of a flow [10], where U and L are the characteristic velocity field and length scale.

Actual values of Re characterizing the flow at the smallest resolved scales are not *a priori* available in coarse grained simulation (CGS), such as LES or ILES where the smallest characteristic resolved scale is determined by the resolution cutoff wavelength prescribed by an *explicit or implicit* spatial-filtering process. Using grid-dependent spatial filtering is the common feature of state-of-the-art practical CGSs, such as ILES. Since the small-scale cutoff is determined by grid size, the implication is that grid refinement is associated with observing smaller simulated physical structures on a somewhat different problem with higher effective Re ($\mathrm{Re}_{\mathrm{eff}}$), e.g., Refs. [11,12]. Extensive ILES applications in engineering, geophysics, meteorology, and astrophysics have been reported [9]. Yet, an important and unique issue is still outstanding for ILES: How one can estimate the values of the relevant effective viscosity (ν_{eff}) produced by the numerical method. It is critical to make progress on this matter, and further formalizing the perceived abilities of ILES in computing high Re flow would, indeed, offer significant values.

In particular, it would be highly desirable to be able to estimate a characteristic ILES $\mathrm{Re}_{\mathrm{eff}}$ (therefore, a relevant ν_{eff}) so that the impact of resolution on predicted flow quantities can be characterized based on using suitable turbulence metrics. This issue becomes especially important when one considers the time-dependent turbulent flows [13,14] induced by Rayleigh-Taylor and Richtmyer-Meshkov instabilities (RMIs) [12,15]. An estimation of ν_{eff} and $\mathrm{Re}_{\mathrm{eff}}$ is critical for determining whether a flow of interest has achieved the minimum state [16] and to assess convergence of macroscopic flow features. As will be shown in the paper, the key to accurately estimating ν_{eff}

is to find a way to do so away from the smallest scales of the simulated flow where the numerically controlled dissipation takes place. It is the goal of this paper to develop such a methodology based on the recently improved understanding on the energy transfer process.

This paper is organized as follows. In Sec. II, the modern energy transfer dynamics, which forms the foundation of our analysis, will be inspected first. The procedure for estimating the numerical viscosity for ILES will be developed, first for two special canonical cases and, second for general complex flows. Section III will offer several illustrative examples on how the methodologies developed can be implemented. A discussion and conclusions will be presented in Sec. IV.

II. NUMERICAL VISCOSITY

The momentum equation for ILES can be written as

$$\frac{\partial(\rho u_i)}{\partial t} = f_i + N_i - D_i, \tag{2}$$

where ρ is the mass density, u_i is the velocity, and N_i is the nonlinear (quadratic, pressure, and dilatation) contributions. Also, when an external agent exists, f_i represents the forcing function. Obviously, f_i equals zero for a decaying turbulence. The numerical dissipation D_i appears here explicitly to represent dissipation effects introduced by the numerics in the spirit of the *modified* equations [2]—the equations whose continuous solution closely approximates the (*computed*) discrete solution of the numerical algorithm underlying the simulation model.

From the transport equation for the kinetic energy K,

$$\frac{dK}{dt} = P + \Lambda - \varepsilon, \tag{3}$$

the *implicit* dissipation rate ε can be obtained. Here, P is the production term, and Λ is the nonlinear transfer term. It should be noted that the *implicit* dissipation rate ε not only includes the dissipation D_i associated with the numerics, but also incorporates that from the energy-containing and inertial ranges. The algorithm used by the researchers should allow minimizing the numerical dissipation of the large scales by maximizing the spectral resolution.

As already mentioned, some aspects of the small scales in the ILES calculations are implicitly controlled at the SGS level. Therefore, it is highly desirable to develop our scheme based on the measurements least influenced by the SGS aspects. Instead, the dynamics of the large scales controls the straining and sweeping motions of the small scales [17]. The estimation of the viscosity based on large-scale measurements would also allow one to incorporate the additional time scales associated with the external agencies [18].

The next step in our development is to utilize the results from the energy transfer studies [19–26]. For DNS or ILES, in order for inertial range dynamics to be independent of both the large-scale energetics and the viscous dissipation, a wide-scale separation must exist between the energy-containing scales and the dissipation spectra in the wave-number space (for a detailed discussion, see Zhou [16] and Zhou *et al*. [27]).

The flux rate of energy $\Pi(k)$ across a wave-number scale k is the most basic measure of the energy transfer process. In the Kolmogorov theory of the universal equilibrium range, it is the only link between the energetic and the dissipative scales of motion [10,21]. Indeed, this direct association makes it possible to estimate the effective dissipation ε, a small-scale measurement, only using large-scale flow field data. The energy transfer function can be constructed by formally multiplying the velocity field to the momentum equation Eq. (2); the spectral energy transfer function can then be obtained by taking the appropriate Fourier transformation for various flow fields. For homogeneous isotropic turbulence, it takes the form [21]

$$\frac{\partial E(k,t)}{\partial t} = F(k,t) + T(k,t), \tag{4}$$

where $F(k)$ denotes the forcing spectrum and $T(k)$ is the energy transfer function. The direct association between the inertial range spectrum and the "ideal" energy transfer process makes it possible to estimate an effective dissipation ε. Contributions to the total flux from the various scale interactions can be written as

$$\Pi(k) = -\int_0^k T(k)dk, \tag{5}$$

and the effective dissipation is

$$\varepsilon = \Pi(k^*) = -\int_0^{k^*} T(k)dk, \tag{6}$$

where k^* is chosen at which wave number the energy flux has achieved a constant value. The accuracy of Eq. (6) for sufficiently high Re can be demonstrated using the DNS of forced isotropic turbulence (see, e.g., Fig. 4 of Kaneda *et al*. [28]).

Once the dissipation rate is obtained, ν_{eff} can be written down, based on a dimensional argument. Since ILES is applied to a broad range of engineering and scientific applications, a scheme should be developed in the physical space. In this fashion, ν_{eff}can be written as

$$\nu_{\text{eff}} = \varepsilon/\Omega, \tag{7}$$

where Ω is the enstrophy $\Omega = \omega^2/2$ and the vorticity $\omega = \nabla \times \boldsymbol{u}$ can readily be evaluated based on the simulated velocity $\boldsymbol{u}$ data.

Consistent with our dimensional estimate—Eq. (7), a ν_{eff} computation strategy for forced isotropic turbulence, was proposed [29] based on

$$\nu_{\text{eff}} = \varepsilon_s/[2\langle s_{ij}s_{ij}\rangle_T], \tag{8}$$

where ε_s denotes the dissipation imposed by the forcing scheme, $\langle\rangle_T$ denotes the volume-time average, sum over repeated roman indices is assumed, $s_{i,j} = (u_{i,j} + u_{j,i})/2$ is the strain tensor, and $()_{,i} = \partial()/\partial x_i$. A later paper by Aspden *et al*. [30] also tackled the same problem; their proposed ν_{eff} had a structure similar to that of Eq. (7),

$$\nu^{\#} = \varepsilon^{1/3}\xi^{4/3}(\Delta x)^{4/3}, \tag{9}$$

where Δx is a characteristic computational cell width, ξ is a dimensionless parameter,[1]

$$\xi = 0.203N^{0.102}, \tag{10}$$

[1]Instead of ξ, Aspden *et al*. [30] use Π—which we use here for the energy flux $\Pi(k)$.

and N is the number of computational cells across the integral length scale. The ν_{eff} computation based on Eqs. (9) and (10) puts a special emphasis on (grid level) small-scale aspects of the simulated flow, which differs philosophically from the computation of ν_{eff} through Eq. (8) based on (*resolved*) small-scale dissipation features.

In what follows, two special cases provide computable values of the dissipation rate directly: the noted steady forced turbulence case (Sec. II A) and transitional and decaying turbulent flow (Sec. II B). The remaining task is to find a practical way to evaluate the dissipation for the complex flow cases (Sec. II C).

A. Forced and decaying turbulence

For forced isotropic turbulence, the target dissipation ε_s is imposed by the forcing scheme, and ν_{eff} can be computed through Eqs. (7) and (8). For decaying turbulence, the numerical Re can be obtained more efficiently in a different fashion. Note that the total energy is dominated by the contributions from the energy-containing scales and the energy decaying equation can be cast into a nondimensional form in terms of the characteristic velocity and length scales U and L,

$$\frac{dK^*(t)}{dt} = -\frac{\Omega^*}{\text{Re}}, \tag{11}$$

where

$$K^* = \frac{K}{U^2}, \tag{12}$$

$$t^* = t(U/L), \tag{13}$$

and Ω^* is the nondimensional enstrophy (see, e.g., Sec. III B). Both the energy decay rate on the left hand side of Eq. (11) and the enstrophy can be computed based on resolved flow quantities in the ILES simulation. For reference, the energy decay rate can also be obtained from DNS databases with various known Re's. The Re_{eff} of ILES can be determined via

$$Re = -\Omega^* \left(\frac{dK^*(t)}{dt^*}\right)^{-1}, \tag{14}$$

and the corresponding effective viscosity can be estimated based on Eq. (1).

It should be stressed that, although the approach just articulated for decaying turbulence is somewhat distinctive from that of the forced flows, the philosophy behind it is the same. An accurate evaluation of the numerical viscosity or Re must be carried out based on measurements that are dominated by the energy-containing scales.

B. Complex flows

The turbulent flows of practical interest are usually both high Re and complex. Yet, as a first cut, an interesting scheme can be developed from the following procedure: (1) For a highly resolved ILES flow, the compensated inertial range occurs at lower spectral ranges. The bottleneck occurs as a plateau at higher wave numbers [31–36]. (2) The flux is still the only link between the energetic and the dissipative scales of motion. (3) The effective dissipations of the computations can be obtained directly from the inflow profiles of the inertial range energy transfer.

Hence, a methodology should be advanced to estimate the "input" of the energy into the energy transfer from the large scales. The key is to carry out this estimation around the energy-containing scales so that the small-scale information where the dissipation is controlled by the numerical methods is not needed. Fortunately, the characteristic time scale of the energy-containing eddies U/L should be on the same order of magnitude as the time scale of the energy-dissipation rate ε/U^2. Based on dimensional ground, a dimensionless ratio D can be introduced as

$$D = \varepsilon L/U^3. \tag{15a}$$

Recently, a significant amount of work has been devoted to investigate the behavior of D as a function of Re [28,32,37,38]. A large body of experimentally and numerically generated data suggested that a nondimensional parameter, such as D, approaches a constant when Re becomes sufficiently large (e.g., Fig. 1). We note that the outer-scale- (L) based Re is approximately related to the Taylor microscale Re_λ [39,40] by $\text{Re}_\lambda \approx (20/3)^{1/2}\sqrt{\text{Re}_L}$ in isotropic flow and by

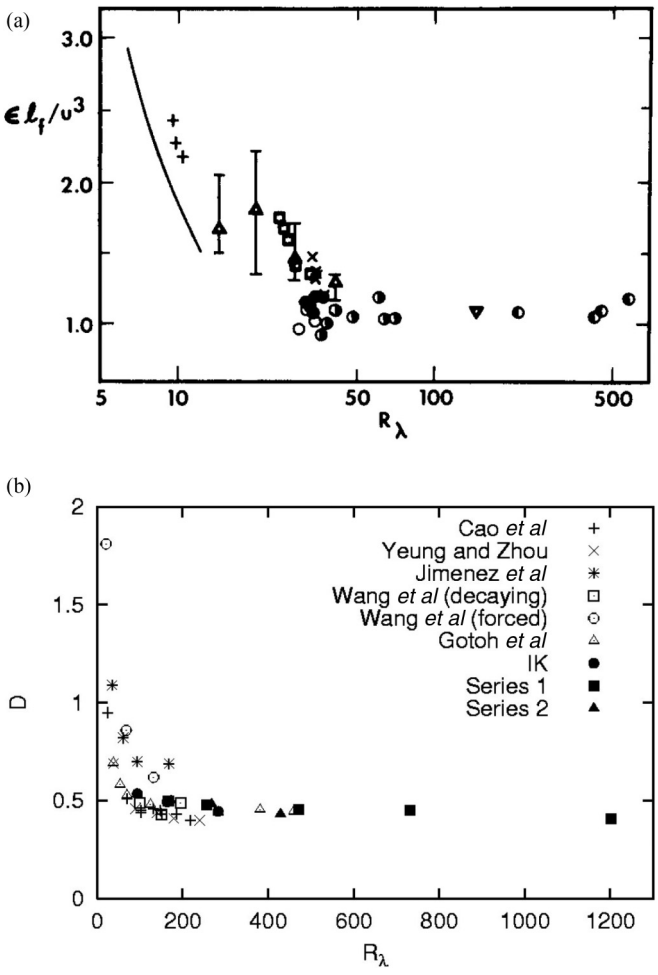

FIG. 1. Nondimensional parameters: (a) $\varepsilon l_f/u^3$ based on laboratory data—from Ref. [37] with l_f denoting a longitudinal integral scale; (b) $D = \varepsilon L/u^3$based on computational simulation data—from Ref. [28] with L denoting the integral scale.

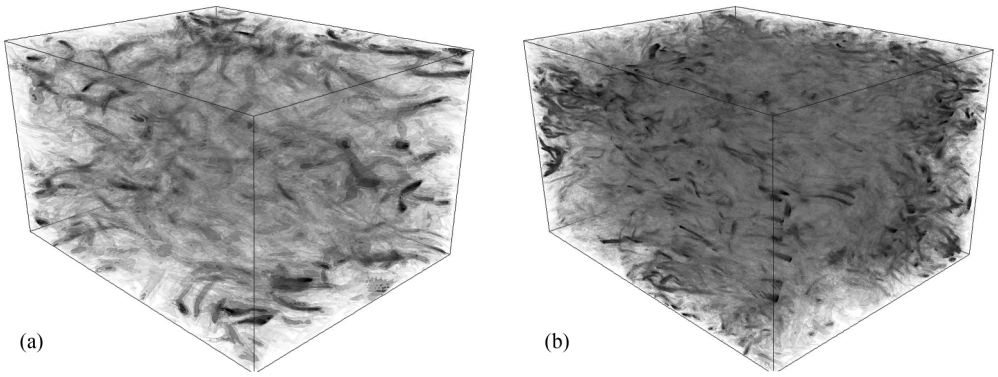

FIG. 2. Isosurfaces of vorticity magnitude scaled by the vorticity rms for ILES of forced turbulence at the finest two grid resolutions: (a) 128^3, (b) 256^3.

$\mathrm{Re}_\lambda \approx 1.4\sqrt{\mathrm{Re}_L}$ for turbulence in the far field of a jet. The literature shows internal consistency between the establishment of an inertial range and the asymptotic behavior of $D \to D_\infty =$ constant. The laboratory data compiled by Sreenivasan [37] exhibited constancy for $\mathrm{Re}_\lambda > 100$. The collection of computational data by Kaneda *et al.* [28] and Sreenivasan [38] indicated that somewhat higher Re_λ is needed, perhaps around 200, for which the inertial range is about 1 decade (e.g., Ref. [32]); observed data scatter for lower Re [e.g., in Fig. 1(b)] has been attributed [38] to differences among forcing schemes, forced long-wavelength ranges, and box sizes. These results depict the (viscosity-independent) energy-dissipation-limit law for high (*but finite*) Re—e.g., Frisch [41] and Sreenivasan [38]. At a high Re limit, the energy flux can be estimated directly,

$$\varepsilon = D_\infty U^3/L. \tag{15b}$$

Recent high-resolution ILES [12,15,29,42,43] shows a limited inertial range of the kinetic energy spectrum as well as distinct flow features associated with high Re flows. The viscosity-independent dissipation rate may have been, thus, captured for these high-resolution ILES flows, and a dimensional estimation, such as $\nu_{\mathrm{eff}} = \varepsilon/\Omega$—through Eq. (7)—may provide a reasonable ν_{eff} in this context. These ideas are the particular focus in the present paper.

III. CASE STUDIES

Here, several flows of increasing complexity will be inspected: Forced homogeneous isotropic turbulence, the evolution of the Taylor-Green vortex (TGV), and a laser-driven reshock experiment. Through these illustrative examples, a case is made for the capabilities of the procedure presented in the previous section for estimating the ILES ν_{eff} and $\mathrm{Re}_{\mathrm{eff}}$.

A. Forced isotropic turbulence

1. Problem description

Positive evaluations of the ILES of forced and decaying isotropic turbulence were reported [42–47]. Comparisons of instantaneous probability distribution functions (PDFs) of explicit (LES) and ILES SGS viscosities in Ref. [29]—computed with Eq. (8)—showed similar behaviors sensitive to the actual SGS models involved, and cumulative distribution functions of the vorticity and strain-rate magnitudes from ILES and LES were in good agreement with those of the DNS of isotropic turbulence. Domaradzki *et al.* [44] and Thornber *et al.* [46] reported well-behaved ILES spectral eddy viscosities in agreement with theory. In contrast, poor performances in this fundamental context were reported by Garnier *et al.* [47] using *finite difference* (rather than FV) discretizations of popular shock capturing schemes.

Here, we consider FV-FCT-based ILES of compressible isotropic turbulence [48], based on using the forcing scheme recently proposed in Ref. [49]. The equations describing the modeled system in a triple periodic domain are the following:

$$\begin{aligned} \rho_{,t} + (\rho u_j)_{,j} &= 0, \\ (\rho u_i)_{,t} + (\rho u_i u_j)_{,j} + p_{,i} &= f_i, \\ E_{,t} + [(E+p)u_j]_{,j} &= 0, \end{aligned} \tag{16}$$

where p is the pressure, $E = \rho u_j u_j/2 - p/(\gamma - 1)$ is the total energy density, $\gamma$is the ratio of specific heats, and an ideal gas equation of state is assumed. Two separate cases were considered with turbulent Mach numbers $\mathrm{Ma} = U/(\gamma p/\rho)^{1/2}$ with $\mathrm{Ma} \sim 0.27$ and 0.13, where U is the root-mean-square (rms) value of the velocity fluctuations evaluated from $3(U)^2 = \langle u_i^2 \rangle_T$ and $\langle\rangle_T$denotes the time-volume mean.

Time-dependent three-dimensional (3D) compressible flow simulations were performed with 32^3, 64^3, 128^3, and 256^3 resolutions using the adaptively refined magnetohydrodynamics solver (ARMS) code for grid-adaptive time-dependent 3D compressible flow simulations [50] with triple-periodic boundary conditions enforced on a cubical domain and a uniformly spaced computational grid; ARMS uses a multidimensional 3D FCT algorithm which is spatially fourth-order accurate in space and second-order accurate in time. Figure 2 exemplifies the developed vorticity field for the 128^3 and 256^3 resolutions, depicting flow dominated by elongated structures characteristic of high Re isotropic turbulence.

PDF analysis associated with isotropic turbulence has been reported for DNS (e.g., Refs. [51,52]) and has been used extensively as a validation tool for ILES (e.g., Refs. [29,43,48,53]). The basic ideas are illustrated in Fig. 3 in terms of the PDFs of characteristic velocity function measures. PDF trends with increasing ILES resolution are the same as for the increasing Re of the DNS data, suggesting a $\mathrm{Re}_{\mathrm{eff}}$

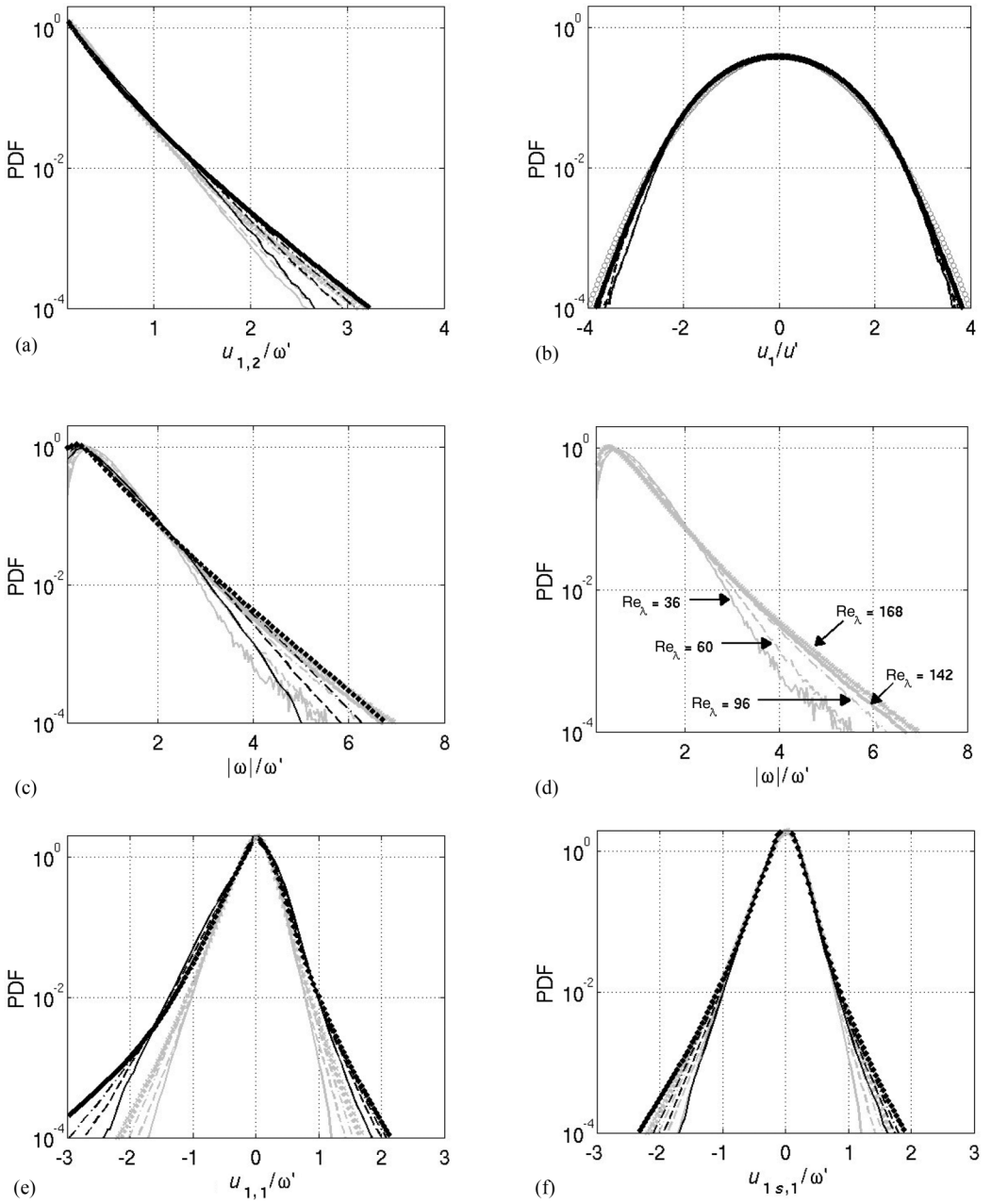

FIG. 3. PDF velocity analysis shows trends with varying Re predicted with DNS as a function of grid resolution. ILES (black)—solid line: 32^3; dashed line: 64^3; dot-dashed line: 128^3; and diamond: 256^3. DNS by Jiménez *et al.* [51] (gray)—solid line: $\mathrm{Re}_\lambda = 36$; dashed line: $\mathrm{Re}_\lambda = 60$; dashed-dotted line: $\mathrm{Re}_\lambda = 96$; diamonds: $\mathrm{Re}_\lambda = 142$; and X: $\mathrm{Re}_\lambda = 168$; $\omega' = \omega_{\mathrm{rms}}$ and results are for the Ma = 0.27 case. (a) Transverse velocity derivatives, (b) velocity fluctuations, (c) and (d) vorticity magnitude, and (e) and (f) longitudinal velocity derivatives. PDFs of longitudinal velocity derivatives are based on the full velocity field in (e), whereas, the corresponding figure (f) is based only on its solenoidal part; the solenoidal velocity is extracted by inverse-Fourier transforming after a Helmholtz decomposition of the velocity field in Fourier space.

for ILES determined by grid resolution. Of considerable interest in the context of assessing resolution as relevant to ILES *convergence* is the fact that PDFs associated with the DNS data approach what appears to be a high Re limit above the mixing transition threshold $\mathrm{Re}_\lambda \approx 100$ [54] [e.g., Fig. 3(d)]. As $\mathrm{Re}_{\mathrm{eff}}$ is increased, the SGS modeling implicitly provided by a well designed ILES numerics consistently captures expected asymptotic turbulence characteristics, such as the Gaussian behavior of fluctuating velocity [Fig. 3(b)] and the non-Gaussian PDF tails of its derivatives [Figs. 3(a) and (e)]; a more detailed statistical analysis can be found in Ref. [48].

The established negative bias in the PDF of the longitudinal derivatives [51,52] also is captured by ILES [Figs. 3(e) and 3(f)]; this bias is recognized as due to turbulent intermittency and self-amplification of longitudinal velocity increments in isotropic turbulence [52]. Figure 3(e) shows that the tails of the PDFs for the ILES-based longitudinal derivatives are wider than for the DNS (with ILES trending closer to incompressible DNS as the Ma decreases [48]). Figure 3(f) shows significantly

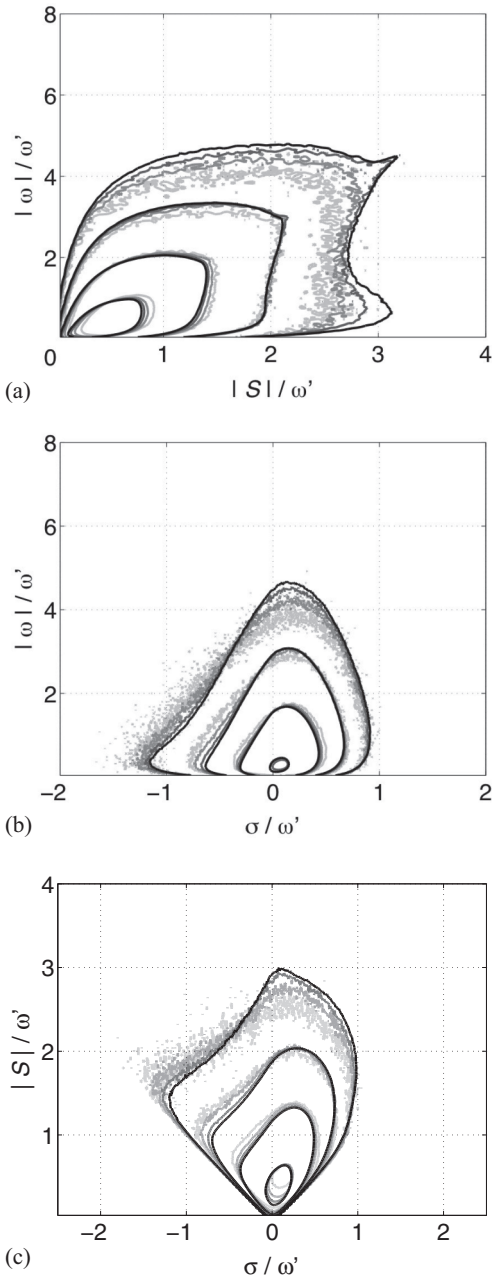

FIG. 4. JPDFs of (a) vorticity magnitude and strain-rate magnitude, (b) vorticity magnitude and vortex stretching, and (c) strain-rate magnitude and vortex stretching. All axes are scaled with the rms vorticity ω'. Increasing darkness corresponds to increasing resolution from 32^3 to 256^3. Contour levels are plotted at 10^{-3}, 10^{-4}, 10^{-5}, and 10^{-6}; results shown are for the Ma = 0.27 case.

improved agreement between ILES and DNS when the PDF analysis is based only on the solenoidal portion of the velocity field. Compressibility mainly affects functions of longitudinal derivatives, whereas, PDFs of transverse derivatives and functions thereof (e.g., vorticity) are less affected by the dilatational velocity [Figs. 3(a) and (c)].

Further (positive) ILES performance aspects are revealed in terms of joint PDFs (JPDFs) of vorticity magnitude ω and magnitude of the strain rate s_{ij}, vorticity magnitude and vortex stretching $\sigma = \omega_i s_{ij} \omega_j / \omega^2$, and strain-rate magnitude

TABLE I. Effective viscosity and Re for the forced turbulence simulations.

Ma	Resolution	ν_{eff} (m^2/s)	Re_λ	$(\text{Re}_\lambda)^2 \sim \text{Re}_L$
0.13	32^3	24.0×10^{-3}	63	3969
	64^3	9.47×10^{-4}	93	8649
	128^3	4.04×10^{-4}	151	22801
	256^3	1.79×10^{-4}	221	48841
0.27	32^3	1.70×10^{-3}	63	3969
	64^3	7.47×10^{-4}	93	8649
	128^3	3.21×10^{-4}	145	21025
	256^3	1.35×10^{-4}	225	50625

and vortex stretching (Fig. 4). These two-dimensional statistics depict a weak correlation between strong vortices and high strain, whereas, high vortex stretching is associated more with moderate levels of vorticity magnitude, not the intense vortices that create wormlike structures. JPDF shapes, trends as functions of grid resolution and depicted weak correspondence between strain-rate magnitude and vortex stretching are in close agreement with those in Ref. [51] as a function of Re; a somewhat wider strain-rate data spread than for the incompressible DNS [51] in Fig. 4(a) is associated with the noted effects of compressibility on the distributions of longitudinal velocity derivatives (also affecting the strain rate [48]).

2. *Effective viscosity and Reynolds number*

The ν_{eff} can be computed through Eq. (8); the effective Re_λ then is computed as $\text{Re}_\lambda = U\lambda/\nu_{\text{eff}}$ with the Taylor microscale of the velocity (λ) fluctuations computed in terms of resolved velocity by

$$\lambda = \frac{1}{3} \sum_{\beta=1}^{3} \sqrt{\langle u_\beta^2 \rangle / \langle (u_{\beta,\beta})^2 \rangle}. \tag{17}$$

The effective viscosity and Re_λ (Table I) are found to approximately scale with power-law fits of the grid spacing h as $\nu_{\text{eff}} \sim h^{1.2}$ and $\text{Re}_\lambda \sim h^{-0.6}$, respectively; the results suggest that the mixing-transition threshold $\text{Re}_\lambda \sim 100$ effectively is crossed (for ILES based on this particular numerics) between the 64^3 and the 128^3 grid resolutions. Yet, the flow has not achieved the $\text{Re}_L = 1.6 \times 10^5$ [16,27] needed for the minimum state.

Velocity fluctuation energy spectra and energy flux are presented in Figs. 5 and 6 to illustrate the reasonableness of the estimated Re. Using a Helmholtz decomposition, the instantaneous velocity fluctuation (around the volumetric mean) is split into its solenoidal and compressible components according to $u_i = u_{i_s} + u_{i_d}$ with the condition $u_{j_s},_j = 0$ in physical space translating into the condition $k_j \hat{u}_{j_s} = 0$ in Fourier space. This condition is used explicitly to separate solenoidal and dilatational components of the Fourier velocity transform in the form $\hat{u}_{i_s} = \hat{u}_i - \hat{u}_{i_d}$ with $\hat{u}_{i_d} = (\hat{u}_j k_j) k_i / k^2$. The spectra in Fig. 5 depict a short solenoidal inertial range consistent with the Kolmogorov $k^{-5/3}$ power law and corresponding compressible contributions which are significantly less; a small region of scale separation between energy-containing and

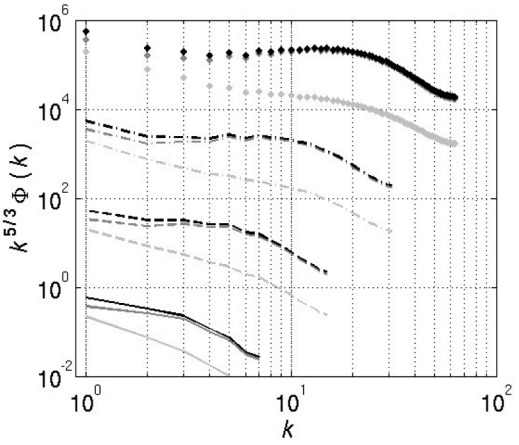

FIG. 5. Compensated velocity energy spectra. Light gray: dilatational component; dark gray: solenoidal component; black: total. Solid line: 32^3; dashed line: 64^3; dashed-dotted line: 128^3; and diamonds: 256^3. Each compensated spectra plot is offset by 2 decades from the resolution below; results shown are for the Ma = 0.27 case.

dissipation scales begins to exist at 128^3, becoming longer for the finer resolution (higher $\mathrm{Re}_{\mathrm{eff}}$) 256^3 case. Consistent with the latter results and Eq. (6), Fig. 6 shows energy flux approaching a constant value—the solenoidal target dissipation set by the forcing for the 256^3 case.

Figure 5 also suggests consistency of the 3D velocity spectra with a power law shallower than $k^{-5/3}$ in the near-dissipation region (the *bottleneck* effect); this feature of the spectra is a standard prediction in DNS (e.g., Refs. [51,52]) and is recognized to be a characteristic feature of solutions of the Navier-Stokes equations for high (but finite) Re—to be captured by a (sufficiently resolved) CGS strategy. The near-dissipation *bump* was captured quite robustly with ILES in high-resolution studies of isotropic turbulence [55] and turbulent jets [56]. Occurrence of the *bump* has been attributed

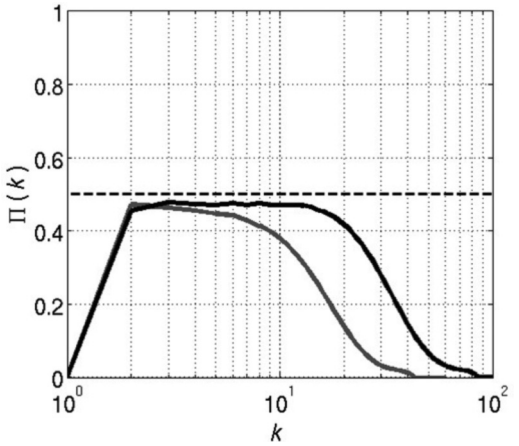

FIG. 6. Energy flux for FCT-based ILES of forced isotropic turbulence at 128^3 (gray) and 256^3 (black) resolutions for the Ma = 0.27 case; the dashed line approximately indicates the solenoidal target dissipation set by the forcing scheme ($\varepsilon_s \sim 0.5$)—the same for both resolutions.

to backscatter effects associated with the presence of worm vortices at the smallest resolved scales [55].

B. Simulated transition and decaying turbulence

1. Problem description

The TGV is a well-defined flow that has been used as a prototype for vortex stretching, instability, and production of small-scale eddies to examine the dynamics of transition to turbulence based on DNS [41,57,58]. The TGV case has also been used to demonstrate how convective numerical diffusion effects of certain algorithms can effectively be used *by themselves* to emulate the dominant SGS physics of transition to turbulence for high (*but finite*) Re flows [11]. ILES strategies were verified in the TGV context for a wide range of monotonic numerics over uniform grids, including Eulerian (characteristics-based Godunov, varying-accuracy FCT [59] with or without directional splitting) and van Leer-based Lagrange-remap algorithms (see Ref. [11]). The studies demonstrated that ILES can robustly capture the (DNS predicted) kinetic energy dissipation rates around a nondimensional transition time; this is exemplified in Fig. 7(a) where slight effects of varying implicit SGS model specifics also are apparent.[2] Our focus in what follows is further characterizing the resolution-dependent $\mathrm{Re}_{\mathrm{eff}}$.

The ability of FCT algorithms to provide predictive under-resolved simulations of the large-scale dynamics of turbulent velocity fields with no free parameters and without SGS models has been documented extensively (e.g., Ref. [11] and Chap. 8 in Ref. [9]). FCT-based ILES of the TGV was carried out using the ARMS code mentioned above [50]. In this context [12], we also recently used the radiation adaptive grid Eulerian (RAGE) code [60] which solves the multimaterial compressible conservation equations for mass density, momenta, total energy, and partial mass densities, using a second-order Godunov scheme; in turn, RAGE has been verified extensively and has been validated against a wide variety of analytic test problems and detailed experiments (e.g., Refs. [12,15]). As used, ILES models high Re convection-driven flow with resolution dependent ν_{eff} determined by the numerical simulation algorithm [11,12].

The TGV configuration involves triple-periodic boundary conditions enforced on a cubical domain with a box side length of 2π cm and a uniformly spaced computational grid. The flow is initialized with the solenoidal velocity field,

$$\begin{aligned} u &= +u_o \sin(kx)\cos(ky)\cos(kz), \\ v &= -u_o \cos(kx)\sin(ky)\cos(kz), \\ w &= 0, \end{aligned} \tag{18}$$

and the pressure is a solution of the Poisson equation for the above given velocity field, i.e.,

$$p = p_o + \frac{\rho(u_o)^2}{8}\left[1+\cos(2kz)\right]\left[\cos(2kx)+\cos(2ky)\right]. \tag{19}$$

[2]Following modified equation analysis [2,3], the corresponding performance of classical LES methods [11] is sensitive to the *combined* explicit *and* implicit SGS model specifics.

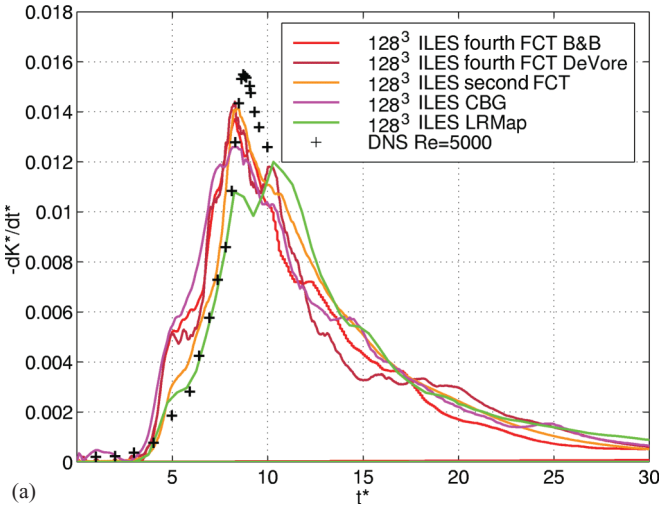

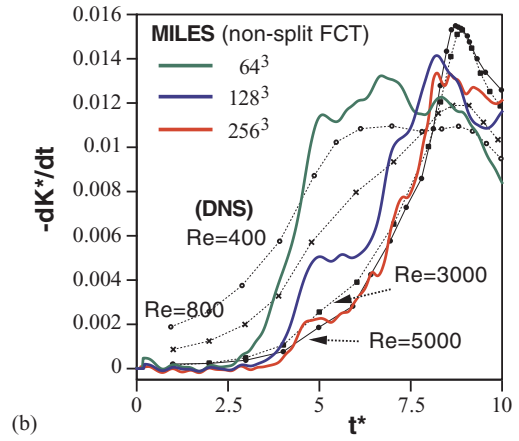

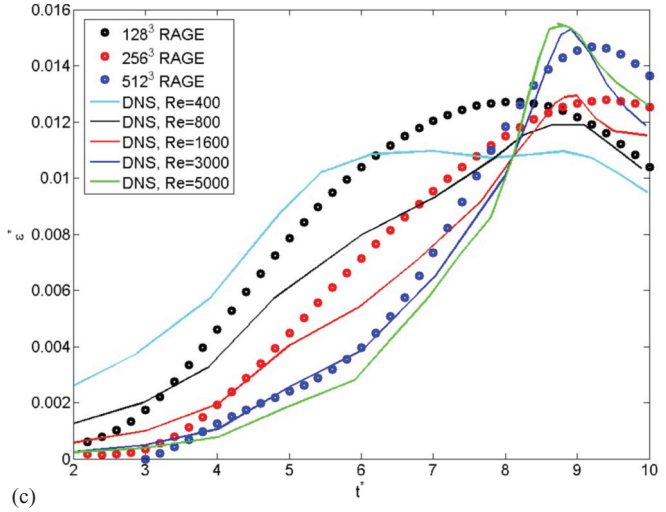

FIG. 7. (Color online) TGV kinetic energy dissipation with ILES based on various different numerics and implementations compared with DNS [57,58]: (a) Eulerian (third-order characteristics-based Godunov, split and nonsplit second-order and fourth-order FCT) vs third-order van Leer-based Lagrange remap on a fixed uniform 128^3 grid—from Ref. [11], (b) fourth-order nonsplit FCT vs resolution—from Ref. [11], and (c) second-order RAGE Godunov vs resolution—from Ref. [12]. The Re is based on the integral scale.

An ideal gas equation of state, STP conditions, unity wave number k, and Ma $= 0.28$ are chosen. Analysis is carried out in terms of appropriate nondimensional variables, e.g., $x^* = kx$, $t^* = ku_o t$.

2. *Effective viscosity and Reynolds number*

The mathematical flow simulation model is based on the conservation equations of mass, momentum, and energy. ILES models tested in Ref. [11] examined *nominally* inviscid flow (Euler based as also considered here) or a linear viscous flow for which SGS effects are neglected (Navier-Stokes based). $\mathrm{Re}_{\mathrm{eff}}$-dependent effects are clearly suggested in Figs. 7(b) and 7(c). Coarser-grid results are associated with wider peaks occurring at lower t^*, a trend that is consistently exhibited by the DNS results as Re is lowered. Moreover, we also find a consistent correlation between scaled profiles of nondimensional mean kinetic energy dissipation rates $-dK^*/dt^*$and enstrophy $\Omega^* = \frac{1}{2}\langle\omega^2\rangle/(kU^2)$, where $K^* = K/U^2$[11]. Peak Ω^* values increase with grid resolution, and the observed correlation between $-dK^*/dt^*$ and Ω^* is consistent with the relation $-dK^*/dt^* = -\Omega^*/\mathrm{Re}$ for an incompressible NS fluid (see also Sec. II A). For a given grid resolution, the suggested $\mathrm{Re}_{\mathrm{eff}}$ values are somewhat higher here for FCT than RAGE-based ILES (based on visual comparisons with the DNS in Fig. 7)—reflecting $\mathrm{Re}_{\mathrm{eff}}$ sensitivities to the details of the SGS model provided implicitly by the numerics and its actual implementation [11].

We can explicitly compute the ν_{eff} and a Taylor microscale as in Sec. III A, based on the simulated 128^3 and 256^3 TGV data from Ref. [11]; results listed in Table II focus particularly on the relatively late times for which self-similar decaying spectra are observed (Fig. 8) with available inertial ranges consistently becoming longer with increasing resolution (and larger associated $\mathrm{Re}_{\mathrm{eff}}$). It should be noted that the highest Re from DNS (5000) and ILES $\mathrm{Re}_{\mathrm{eff}}$ ($\mathrm{Re}_L \sim 1500$–3000) in the TGV studies [Figs. 7(b), 7(c), and Table II are still on the low side compared to the mixing-transition threshold values from Ref. [54] $\mathrm{Re}_L \sim 1$ to 2×10^4or $\mathrm{Re}_\lambda \sim 100$. This fact also is illustrated in Fig. 8, depicting kinetic energy spectra lacking significant scale separation between the energy-containing and dissipation scales, albeit *suggesting* the near-dissipation bump in the energy spectra as $\mathrm{Re}_{\mathrm{eff}}$ approaches the mixing-transition threshold.

TABLE II. Effective viscosity and Re for FCT-based ILES of the Taylor-Green vortex.

	t^*	ν_{eff} (m^2/s)	Re_λ	$(\mathrm{Re}_\lambda)^2 \sim \mathrm{Re}_L$
128^3	8.85	1.41×10^{-3}	29	841
	19.7	8.64×10^{-4}	21	441
	29.9	5.55×10^{-4}	25	625
	42.9	4.52×10^{-4}	21	441
256^3	9.1	5.55×10^{-4}	52	2704
	19.1	3.40×10^{-4}	38	1444
	30.2	2.14×10^{-4}	44	1936
	39.8	1.78×10^{-4}	41	1681

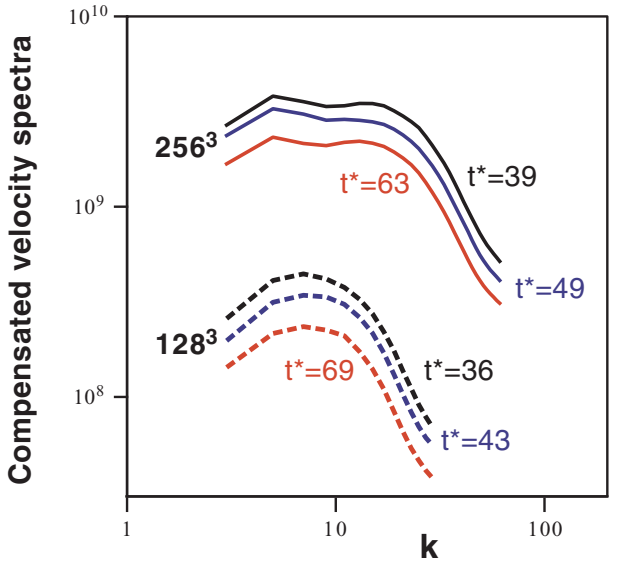

FIG. 8. (Color online) Compensated spectra for the ILES-FCT TGV cases of Table II.

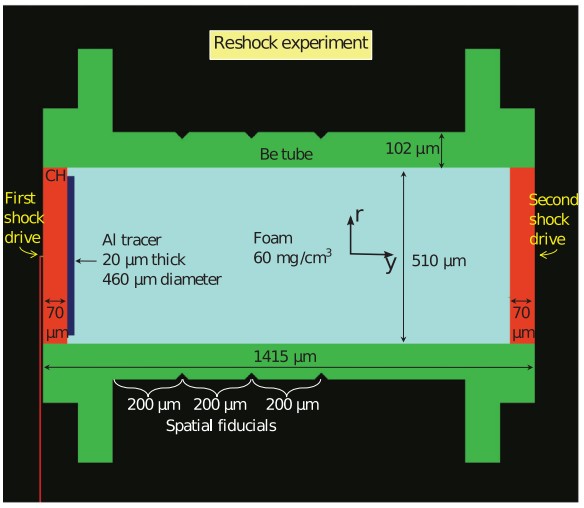

FIG. 9. (Color online) Target geometry.

C. Complex flow example: A laser-driven reshock experiment

1. Problem description

In this section, the Re_{eff} analysis is explored further for a complex flow example involving inhomogeneous features, acceleration, transition and decay, as well as sensitivity to initial condition resolution uncertainties. Turbulence metrics for this kind of flow are not yet established, and the state-of-the-art analysis largely relies on using unsteady versions of diagnostics designed for developed homogeneous isotropic turbulence. Furthermore, our analysis above (Secs. III A and III B) involved a crucial simplifying feature: homogeneous features—which could be approached by enforcing periodicity and using uniformly spaced gridding; accurate spectral and energy flux analysis addressing scale separation is typically not practical when using nonuniform computational grids and resolution refinements in localized regions as in this section.

ILES studies [61] of a laser-driven reshock experiment [62] in the strong-shock high energy density regime were recently carried out to better understand material mixing driven by the RMI. ILES validation was based on direct comparison of simulation and radiographic data. ILES was also compared with published DNS data and the theory of homogeneous isotropic turbulence. Despite the fact that the flow was not homogeneous, isotropic, nor fully turbulent, local regions in which the flow demonstrates characteristics of homogeneous isotropic turbulence were identified by the presence of high levels of turbulent kinetic energy (TKE) and vorticity magnitude. After reshock, the analysis showed results consistent with those for incompressible isotropic turbulence. Self-similarity and Re_{eff} assessments suggested that the results were reasonably converged at the finest resolution.

The laboratory reshock experiments [62] were performed using the University of Rochester's OMEGA laser. The laboratory target consists of a cylindrical beryllium (Be) tube $\approx$1.4 mm in length and $\approx$0.5 mm in diameter with an $\approx$100 μm wall thickness (Fig. 9). The progression of events in the experiment can be visualized in terms of the schematic shock-interface diagram in Fig. 10. The target is successively hit from both sides by two laser-driven shocks. The first, $\approx$5 kJ, at $t = 0$ ns, impacts the plastic ablator on the left, driving a Mach $\approx$5 shock through the 20 μm aluminum (Al) tracer disk adjoining the ablator. The tracer disk is, thus, propelled to the right down the center of the cylinder, which is filled with a low-density (60 mg/cc) CH foam. The second shock, $\approx$4 kJ at 5 ns, impacts a plastic ablator at the right end of the tube. The shocks collide at approximately 8 ns to the right of the mixing layer, and the second shock hits (reshocks) the mixing layer at approximately 10 ns, causing it to compress until approximately 13 ns. At approximately 17 ns, the second shock exits the mixing layer. At later times (beyond the present scope), the mixing layer is further affected by compression or expansion waves, and secondary shocks are generated by reflections at the Be tube interface.

As in previously reported studies of the RMI [12,15,63], ILES used the RAGE code [60] with appropriate equations of state, adaptive mesh refinement (AMR) involving cubic cells, and material interface treatments not activated; ILES, thus,

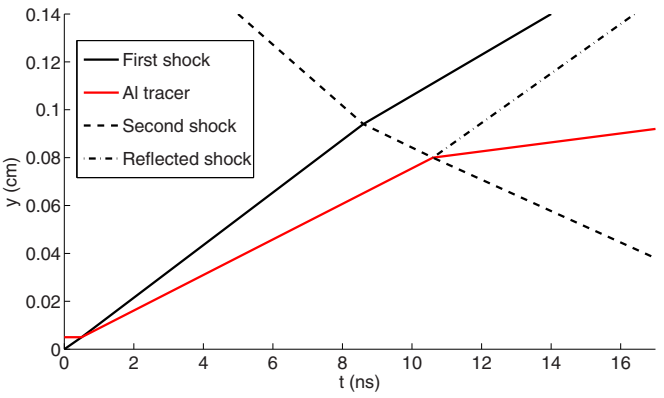

FIG. 10. (Color online) Schematic of a shock-interface diagram depicting the progression of events in the experiment. Crossing locations are approximate.

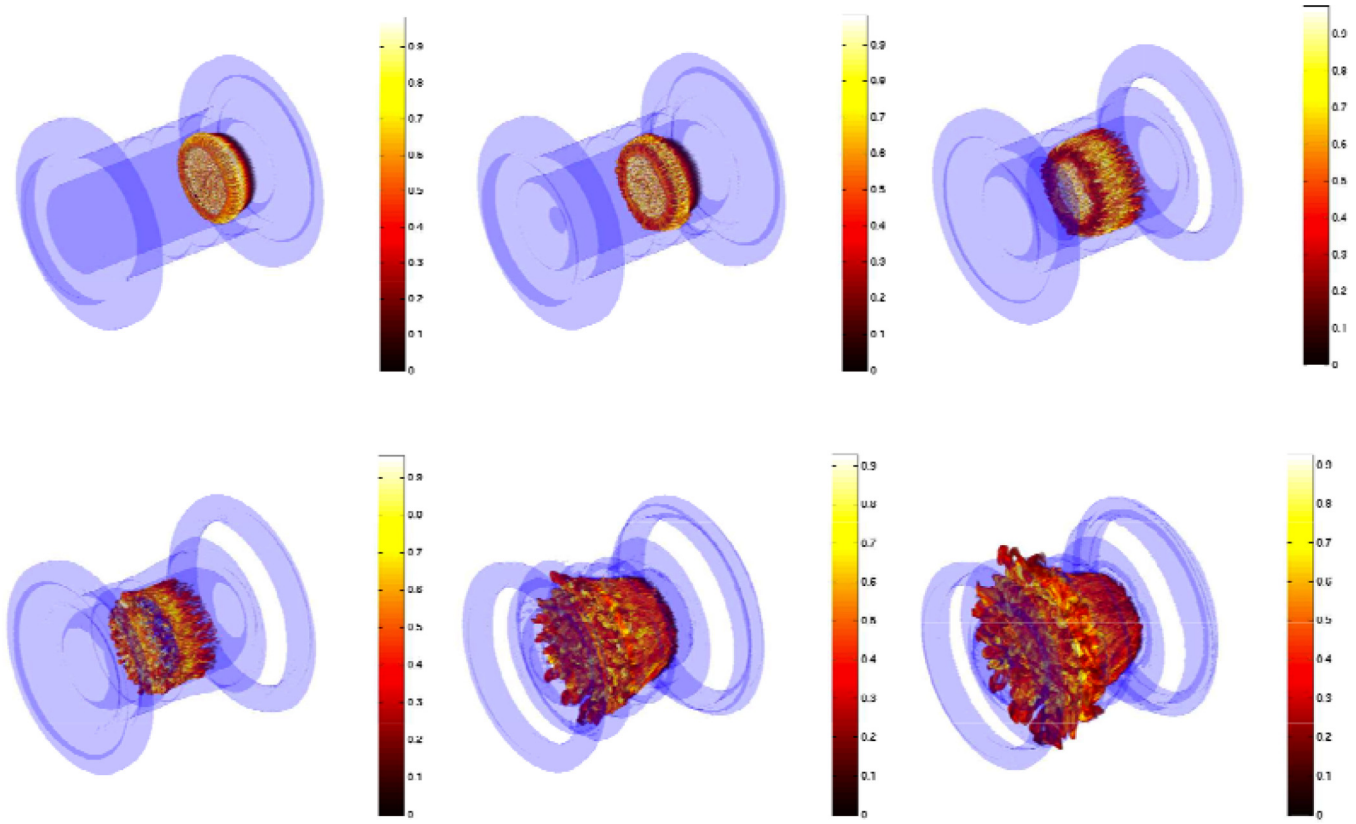

FIG. 11. (Color online) Simulated Al concentration visualization for 2.5 μm resolution data; times (in nanoseconds) from top left to bottom right are $t = 5$, 7, 10 (reshock), 12, 17 (second shock leaves mixing layer), and 20 ns. The semitransparent isosurfaces reflect the approximate location of the Be tube interface.

models high Re miscible flow. As we consider simulating the RMI in laboratory experiments, we must also consider the effects of modeling initial conditions for which limited experimental characterizations are available. The Al interfaces were perturbed using deformations with spectral content and standard deviation emulating typical surface finish characteristics as closely as possible to those in the laboratory samples; a comparable k^{-2} spectrum was used as well for comparison (see Ref. [61]).

Typical visualizations of the simulated Al concentration are shown in Fig. 11. The presence of small-scale features in the data suggests turbulent features in the mixing layers which become more pronounced after reshock ($t \approx 10$ ns). In Ref. [61], we argued that the better match found between the finest (2.5 μm) resolution data and the laboratory experiments was an indication that this simulation had a more appropriate $\mathrm{Re}_{\mathrm{eff}}$—i.e., high enough to expect achieving self-similar characteristics.

RMI-induced turbulent flow is inherently unsteady and involves transitional and decaying turbulence aspects. We mined our simulation database using suitably adapted diagnostics originally designed for statistically steady homogeneous isotropic flow. We take advantage of the cylindrical geometry of the problem, and azimuthal spatial averaging is carried out to evaluate mean quantities; deviations around such mean values are used to characterize relevant statistical fluctuations. The simulations were performed at three maximum grid resolutions (1.25, 2.5, and 5 μm), and all used AMR. The more computer intensive 1.25 μm simulations involved only a quadrant of the whole domain; for reference, a single quadrant 2.5 μm run also was carried out.

Sampling of reshock simulation data focuses on flow regions containing high levels of TKE and/or vorticity—which, as noted, are neither homogeneous nor isotropic. Weak-vorticity distributions associated with the sampled transitional data are very distinct from the isotropic homogeneous data due to their irrotational flow content. In Ref. [61], data filtering based on vorticity content ($\omega > 0.5\omega_{\mathrm{rms}}$) was implemented in order to have meaningful comparative analysis. Such vorticity-based data filtering also was used here to obtain quantitative estimates the characteristic velocity field $U = (2\mathsf{K}/3)^{1/2}$, where $\mathsf{K} = \langle \mathrm{TKE} \rangle$ is the volumetrically averaged specific TKE.

2. *Effective viscosity and Reynolds number*

Asymptotic estimates for an outer scale $\mathrm{Re}_{\mathrm{eff}}$ can also be generated. Following the discussion towards the end of Sec. II, we assume that high Re isotropic turbulence regimes for which $D = \varepsilon L/U^3 \approx \frac{1}{2}$ have been achieved[3] and define a time dependent L to be the outer scale prescribed by a mixing width δ_{MZ}. As in Refs. [12,64], the material mixing zone (MZ)

[3]Following Ref. [28] [Fig. 1(b)], for a high Re, we expect $D \sim 0.5 - 2$ with $D_\infty \approx 0.5$.

thickness δ_{MZ} is defined in terms of the mixedness $M(y)$ by

$$\delta_{MZ} = \int M(y)dy, \tag{20}$$

where

$$\begin{aligned} M(y) &= 4\psi(y)[1-\psi(y)], \\ \psi(y) &= \langle Y_{Al}\rangle, \quad Y_{Al} = \rho_{Al}/\rho, \\ \langle f\rangle(y) &= \int f(x,y,z)dx\,dz / \int dx\,dz, \end{aligned} \tag{21}$$

and ρ_{Al} denotes the Al partial mass density. We can, thus, formulate an *asymptotic* model for the dissipation $\varepsilon = DU^3/(2L)$; in this context, we can now evaluate outer-scale (asymptotic) measures of $\nu_{eff} = \varepsilon/[2\langle s_{ij}s_{ij}\rangle]$ and $\mathrm{Re}_{eff} = UL/\nu_{eff}$. The computed outer-scale-based measures of mixing width ν_{eff} and outer-scale Re_{eff} are plotted in Fig. 12 where observed time shifts between features captured with varying resolutions and different computational domains were compensated for. Time shifts reflect on slightly differently resolved initial interface conditions and their cumulative effects on the flow conditions at reshock time; they also reflect on the fact that only a quadrant of the full domain (and, thus, differently allowed azimuthal constraints and nonlinear mode couplings) was involved in the finest (1.25 μm) resolution simulation. Such differences slightly affect TKE peak times and actual reshock times (Fig. 13) but *not* actual TKE peak values—so that the TKE production mechanisms appear well resolved for the finest two resolutions. Examining the vorticity filtered results vs resolution for times 2–6 ns after the TKE peak, Fig. 12(c) depicts consistent Re_{eff} values between 10^4 and 5×10^4—above the mixing-transition threshold [54] $\mathrm{Re}_L \sim 1$ to 2×10^4 with higher Re_{eff} being associated with finer resolution. Again, we note that the flow has not achieved the $\mathrm{Re}_L = 1.6\times10^5$ [16,27] needed for the minimum state.

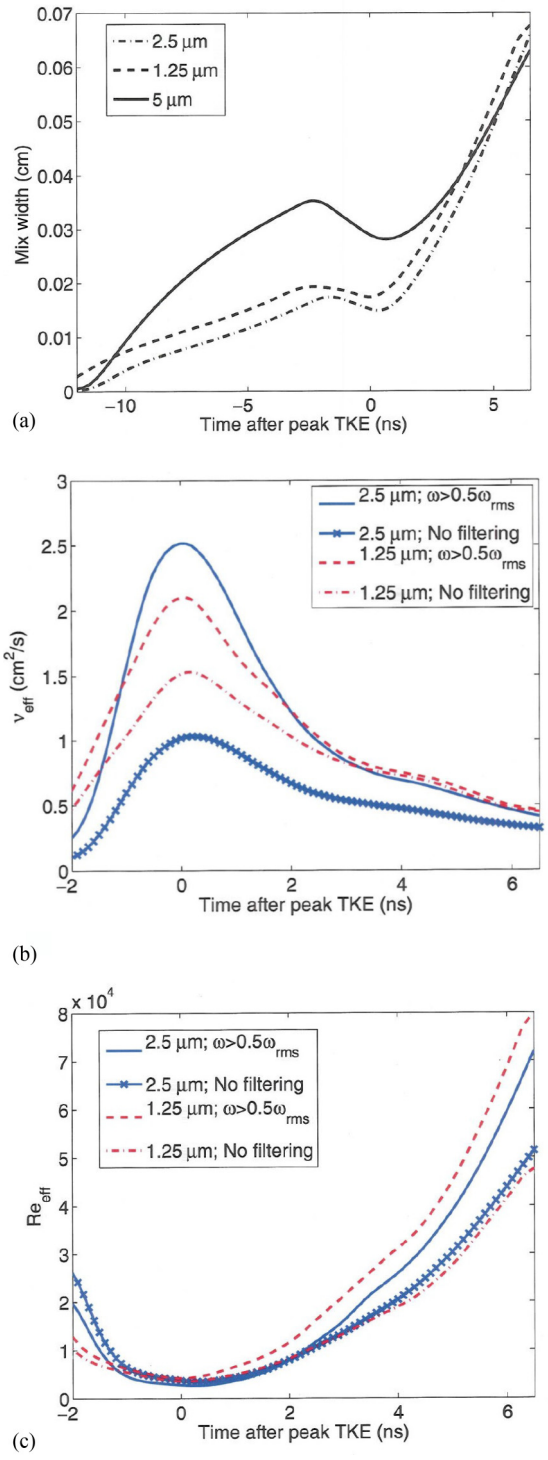

FIG. 12. (Color online) Asymptotic measures of the (a) mixing width (b) ν_{eff}, and (c) outer-scale Re_{eff} are shown.

IV. SUMMARY AND DISCUSSION

This paper focused on developing a framework for estimating the Re of the complex flows computed using ILES. The basic building block of our methodology is to utilize our improved understanding of the energy transfer process for turbulent flows where the existence of the inertial range already is self-evident. Therefore, our approach restricts us to the applications where the scale separation between the energy-containing and dissipation scales has been illustrated. The corollary of above statement is that we are not concerned about these flows where the values of the Re clearly are low as indicated by a simple inspection of their energy spectra. This is extremely appropriate as the strength of the ILES is its potential for capturing the highly turbulent flows of interest for scientific and engineering applications. The low Re flows our method ignored, however, usually can be computed using DNS.

By construction, some aspects of the small scales in the ILES calculations are implicitly controlled at the SGS level as the dissipation of the energy is carried out by the numerical method. The proposed procedures allowed us to sidestep those measurements at the small scale. For those flows where our methodology is applicable, the existence of a universal inertial range implies that, during the energy transfer process, the energy flux is the only link between the energy-containing scale, which controls the dynamics of the flow, and the dissipation range. The dissipation of the energy, therefore, is best estimated from the energy flux, which is evaluated with energy-containing scale measurements. Thus, an important implication is that the ILES numerics and grid resolution

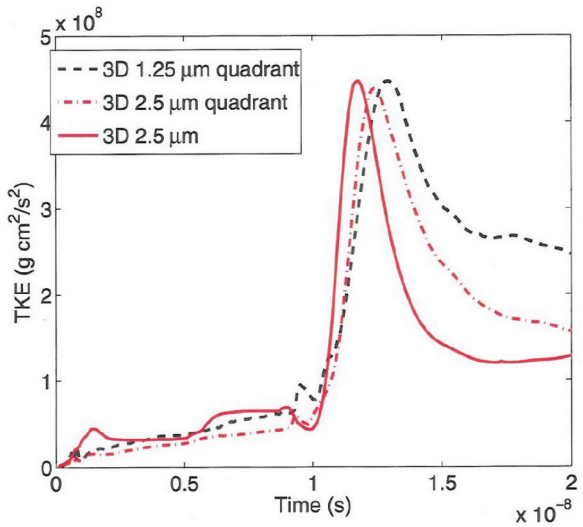

FIG. 13. (Color online) Volumetric integration used to measure turbulent kinetic energy; effects of grid resolution and actual spatial domain (full vs single quadrant) are examined.

should be chosen with great care so that the dissipation from the energy-containing and inertial range scales can sufficiently be reduced to yield high enough Re_{eff} (to capture the viscosity-independent energy-dissipation limit).

We are now at a position to address a practical question the researchers often are confronted with. When is the grid resolution fine enough? The answer, in fact, has already been offered implicitly in previous sections describing our procedure but will be highlighted and will briefly be summarized here for completeness. Again, an existence of an inertial range is a prerequisite for using our method. Once this minimum threshold has been passed, as the length of the inertial range increases, the Re_{eff} can progressively be more and more accurately estimated. With ILES, this improvement can be achieved with increased resolutions. When the inertial range of a given flow can be computed with a sufficient length, the important energy-containing scale would be prevented from being contaminated by the dissipation scale, which is not universal. The critical Re indicating that the sufficient inertial range length has been obtained has been called the minimum state and has been determined as 1.6×10^5 [16]. As long as the grid resolution is fine enough to achieve the minimum state, the investigators can be sure that their numerical simulations have reproduced all of the most influential physics of the flows.

The discussion above naturally leads us to another question regarding the simulation environment for the cases of time-dependent flows. For some complex flows of practical interest, the flow fields may experience several distinctive phases. For instance, the unsteady flows this paper employed as our case studies (the TGV and the reshock problem) involve successive crucial features one typically cares for: (1) transition, (2) some degree of turbulence development, and then, (3) decay. A different example, not considered here, is the turbulence induced by Rayleigh-Taylor instability [see, for example, Refs. [65,66] where the time-dependent flows start from rest and are subject to a constant external forcing, either in the form of the gravity or in the high acceleration. Hence, the second question one must address can be phrased as the following. What is the minimum time for transitioning to the minimum state? More specifically, one can ask in a slightly different fashion: What is the required grid resolution or box size so that the critical time demanded for surpassing the minimum state can be achieved?

A reasonable answer can be obtained based on the time-dependent mixing-transition criterion articulated in Ref. [16]. Several examples have been offered in Refs. [13,14] on the utilization of such a criterion. A number of examples are provided for turbulent flows induced by Rayleigh-Taylor and Richtmyer-Meshkov (single shock) instabilities. The task to carry out these analyses is relatively straightforward—since it is widely accepted that the mixing layer widths of these flows develop as a function of time. The situations become more complicated when both first shock and reshock are involved. For instance, in some inertial confinement fusion applications, a time-dependent mixing width around material interfaces evolves from the initial value and grows very large for strong shocks. If the interface sees a second shock, the mixing again is intensified [66]. The challenge in applying the time-dependent criterion can be alleviated by taking advantage of relevant extended phenomenological treatments as developed in Ref. [67], and the same procedure demonstrated in Refs. [13,14] can be carried out in a straightforward fashion. Of course, not all applications have such simple models already developed and available to the researchers. Nevertheless, high quality experimental databases could be employed instead.

ACKNOWLEDGMENTS

Los Alamos National Laboratory (LANL) is operated by the Los Alamos National Security, LLC for the U.S. Department of Energy NNSA under Contract No. DE-AC52-06NA25396. This work was performed under the auspices of the Lawrence Livermore National Security, LLC under Contract No. DE-AC52-07NA27344 and was made possible by funding from the LANL-LDRD Project No. 20100441ER on "LES Modeling for Predictive Simulations of Material Mixing." We thank H. Aluie for providing the code and assistance to compute the energy flux functions in Fig. 6.

[1] P. Sagaut, *Large Eddy Simulation for Incompressible Flows*, 3rd ed. (Springer, Berlin, 2006).
[2] C. W. Hirt, Phys. Fluids **12**, II-219 (1969).
[3] S. Ghosal, J. Comput. Phys. **125**, 187 (1996).
[4] Y. Zhou, M. Hossain, and G. Vahala, Phys. Lett. A **139**, 330 (1989).
[5] J. A. Domaradzki and N. A. Adams, J. Turbulence **3**, N24 (2002).
[6] S. B. Pope, New J. Phys. **6**, 35 (2004).
[7] J. P. Boris, in *Whither Turbulence? Turbulence at the Crossroads*, edited by J. L. Lumley, Lecture Notes in Physics Vol. 357 (Springer, New York, 1990), p. 344.
[8] J. P. Boris, F. F. Grinstein, E. S. Oran, and R. J. Kolbe, Fluid Dyn. Res. **10**, 199 (1992).
[9] *Implicit Large Eddy Simulation: Computing Turbulent Flow Dynamics*, edited by F. F. Grinstein, L.G. Margolin, and W. G. Rider (Cambridge University Press, New York, 2010), 2nd printing.

[10] G. K. Batchelor, *The Theory of Homogeneous Turbulence* (Cambridge University Press, New York, 1953).
[11] D. Drikakis, C. Fureby, F. F. Grinstein, and D. Youngs, J. Turbulence **8**, N20 (2007).
[12] F. F. Grinstein, A. A. Gowardhan, and A. J. Wachtor, Phys. Fluids **23**, 034106 (2011).
[13] Y. Zhou, H. F. Robey, and A. C. Buckingham, Phys. Rev. E **67**, 056305 (2003).
[14] Y. Zhou *et al.*, Phys. Plasmas **10**, 1883 (2003).
[15] A. A. Gowardhan and F. F. Grinstein, J. Turbulence **12**, N43 (2011).
[16] Y. Zhou, Phys. Plasmas **14**, 082701 (2007).
[17] Y. Zhou, Phys. Rep. **488**, 1 (2010).
[18] Y. Zhou, W. H. Matthaeus, and P. Dmitruk, Rev. Mod. Phys. **76**, 1015 (2004).
[19] M. Lesieur, *Turbulence in Fluids* (Nijhoff, Dordrecht, The Netherlands, 1987).
[20] R. H. Kraichnan, J. Fluid Mech. **47**, 525 (1971).
[21] Y. Zhou, Phys. Fluids A **5**, 2511 (1993).
[22] Y. Zhou, Phys. Fluids A **5**, 1092 (1993).
[23] Y. Zhou, P. K. Yeung, and J. G. Brasseur, Phys. Rev. E **53**, 1261 (1996).
[24] Y. Zhou and C. G. Speziale, Appl. Mech. Rev. **51**, 267 (1998).
[25] T. Gotoh and T. Watanabe, J. Turbulence **6**, N1 (2005).
[26] J. A. Domaradzki, B. Teaca, and D. Carati, Phys. Fluids **21**, 025106 (2009).
[27] Y. Zhou, A. C. Buckingham, F. Bataille, and L. Mathelin, Phys. Lett. A **373**, 2746 (2009).
[28] Y. Kaneda, T. Ishihara, M. Yokokawa, K. Itakura, and A. Uno, Phys. Fluids **15**, L21 (2003).
[29] C. Fureby and F. F. Grinstein, AIAA J. **37**, 544 (1999).
[30] A. Aspden, N. Nikiforakis, S. Dalziel, and J. B. Bell, Commun. Appl. Math. Comp. Sci. **3**, 103 (2008).
[31] G. Falkovich, Phys. Fluids **6**, 1411 (1994).
[32] P. K. Yeung and Y. Zhou, Phys. Rev E **56**, 1746 (1997).
[33] Z.-S. She, S. Chen, G. Doolen, R. H. Kraichnan, and S. A. Orszag, Phys. Rev. Lett. **70**, 3251 (1993).
[34] S. G. Saddoughi and S. V. Veeravalli, J. Fluid Mech. **268**, 333 (1994).
[35] N. Cao, S. Chen, and G. D. Doolen, Phys. Fluids **11**, 2235 (1999).
[36] L. P. Wang, S. Chen, J. G. Brasseur, and J. C. Wyngaard, J. Fluid Mech. **309**, 113 (1996).
[37] K. R. Sreenivasan, Phys. Fluids **27**, 1048 (1984).
[38] K. R. Sreenivasan, Phys. Fluids **10**, 528 (1998).
[39] H. Tennekes and J. L. Lumley, *First Course in Turbulence* (MIT Press, Cambridge, MA, 1972).
[40] P. Sagaut and C. Cambon, *Homogeneous Turbulence Dynamics* (Cambridge University Press, Cambridge, U.K., 2008).
[41] U. Frisch, *Turbulence* (Cambridge University Press, Cambridge, U.K., 1995).
[42] D. H. Porter, P. R. Woodward, and A. Pouquet, Phys. Fluids **10**, 237 (1998).
[43] C. Fureby and F. F. Grinstein, J. Comput. Phys. **181**, 68 (2002).
[44] J. A. Domaradzki, Z. Xiao, and P. Smolarkiewicz, Phys. Fluids **15**, 3890 (2003).
[45] L.G. Margolin, W. J. Rider, and F. F. Grinstein, J. Turbulence **7**, N15 (2006).
[46] B. Thornber, A. Mosedale, and D. Drikakis, J. Comput. Phys. **226**, 1902 (2007).
[47] E. Garnier, M. Mossi, P. Sagaut, P. Comte, and M. Deville, J. Comput. Phys. **153**, 273 (1999).
[48] A. J. Wachtor, F. F. Grinstein, C. R. Devore, J. R. Ristorcelli, and L. G. Margolin Phys. Fluids **25**, 025101 (2013).
[49] M. R. Petersen and D. Livescu, Phys. Fluids **22**, 1 (2010).
[50] C. R. Devore, Naval Research Laboratory Memorandum Report No. 6440-98-8330, 1998 (unpublished).
[51] J. Jiménez, A. A. Wray, P. G. Saffman, and R. S. Rogallo, J. Fluid Mech. **255**, 65 (1993).
[52] Y. Li and C. Meneveau, Phys. Rev. Lett. **95**, 164502 (2005).
[53] Y. Li, E. Perlman, M. Wan, Y. Yang, R. Burns, C. Meneveau, R. Burns, S. Chen, A. Szalay and G. Eyink, J. Turbulence **9**, N31 (2008).
[54] P. E. Dimotakis, J. Fluid Mech. **409**, 69 (2000).
[55] D. H. Porter, A. Pouquet, and P. R. Woodward, Phys. Fluids **6**, 2133 (1994).
[56] F. F. Grinstein, J. Fluid Mech. **437**, 69 (2001).
[57] M. E. Brachet, D. I. Meiron, S. A. Orszag, B. G. Nickel, R. H. Morg, and U. J. Frisch, J. Fluid Mech. **130**, 411 (1983).
[58] M. E. Brachet, Fluid Dyn. Res. **8**, 1 (1991).
[59] *Flux-Corrected Transport, Principles, Algorithms, and Applications*, 2nd ed., edited by D. Kuzmin, R. Löhner and S. Turek (Springer-Verlag, New York, 2012).
[60] M. Gittings, R. Weaver, M. Clover, T. Betlach, N. Byrne, R. Coker, E. Dendy, R. Hueckstaedt, K. New, W. R. Oakes, D. Ranta, and R. Stefan, Comput. Sci. Discovery **1**, 015005 (2008).
[61] B. M. Haines, F. F. Grinstein, L. Welser-Sherrill, and J. R. Fincke, Phys. Plasmas **20**, 022309 (2013).
[62] L. Welser-Sherrill, J. Fincke, F. Doss, E. Loomis, K. Flippo, D. Offermann, P. Keiter, B. M. Haines, and F. F. Grinstein, High Energy Density Phys. **9**, 496 (2013).
[63] B. M. Haines, F. F. Grinstein, and J. D. Schwarzkopf, J. Turbulence **14**, 46 (2013).
[64] D. J. Hill, C. Pantano, and D. I. Pullin, J. Fluid Mech. **557**, 29 (2006).
[65] A. W. Cook and Y. Zhou, Phys. Rev. E **66**, 026312 (2002).
[66] W. Cabot and Y. Zhou, Phys. Fluids **25**, 015107 (2013).
[67] K. O. Mikaelian, Phys. D **240**, 935 (2011).